

Observation of nodal links in momentum space

Erchan Yang^{1, 2†}, Biao Yang^{3†}, Oubo You^{1, 2}, Qinghua Guo⁴, Shaojie Ma^{1, 2}, Lingbo Xia⁵,
Dianyuan Fan¹, Yuanjiang Xiang^{1*}, Shuang Zhang^{2*}

¹International Collaborative Laboratory of 2D Materials for Optoelectronic Science and Technology of Ministry of Education, College of Optoelectronic Engineering, Shenzhen University, Shenzhen 518060, China

²School of Physics and Astronomy, University of Birmingham, Birmingham B15 2TT, United Kingdom

³College of Advanced Interdisciplinary Studies, National University of Defense Technology, Changsha 410073, China

⁴Department of Physics and Institute for Advanced Study, The Hong Kong University of Science and Technology, Hong Kong, China

⁵Center for Terahertz Waves and College of Precision Instrument and Optoelectronics Engineering, Tianjin University and the Key Laboratory of Optoelectronics Information and Technology (Ministry of Education), Tianjin 300072, China

*Correspondence to: yjxiang@szu.edu.cn(Y.X.); s.zhang@bham.ac.uk(S.Z.)

†These authors contributed equally to this work.

Abstract

In crystals, two bands may cross each other and form degeneracies along a closed loop in the three-dimensional momentum space, which is called nodal line. Nodal line degeneracies can be designed to exhibit nodal rings, chains, links and knots. With rich global topological structure and other peculiar properties, such as diverse surface state variations, nodal links have attracted extensive theoretical attentions. However, they impose stringent requirements on the Hamiltonian form and hence have not yet been observed in realistic materials thus far. Here, we propose a simple realization of nodal links in a biaxial hyperbolic metamaterial. The two linked nodal lines threading through each other are formed by the crossings between three adjacent bands. On the interface between the metamaterial and air, surface bound states in the continuum (BICs) are observed, which serve as the symmetry-enforced derivative of drumhead surface states from the linked nodal lines. Our discovery not only experimentally demonstrates the global topological structure of nodal links, but also opens the gate towards manipulating topological surface states.

The research on topological gapless phases focuses on the investigation of various band degeneracies, such as Weyl points, Dirac points and nodal lines (NLs)¹⁻¹⁶. NL semimetals have degeneracy along lines forming closed loop(s) in the three-dimensional momentum space^{2,8}. Their existence usually requires the presence of certain symmetries, such as space-time inversion (*PT*), chiral and mirror symmetries. In a simple mirror symmetric system, the conduction and valence bands with opposite mirror eigenvalues can cross each other on the mirror planes and then mirror symmetry protected NLs are formed^{8,17-19}. A key feature of the NL semimetals is that an eigenstate accumulates a Berry phase of π when adiabatically transporting along a closed path encircling the NL⁸. This can be understood by the local linear band structure expanded near the NL degeneracy, which is topologically equivalent to a two-dimension Dirac cone. When certain symmetries of the system are broken, NL semimetals can transform into other topological phases, such as Weyl, Dirac semimetals and 3D topological insulators²⁰⁻²⁴. In the last few years, the concept of NLs has also been extended to classic systems, leading to extensive research in photonics and phononics/acoustics^{13,25-27}.

New interests are inspired when considering global linking or knotting properties of NLs^{14,17,28-34}. Based on these, NLs have been classified into topological nodal rings (Fig. 1a), nodal chains^{7,13,35-37} (Fig. 1b), nodal links^{14,17,29,30,32,34} (Fig. 1c) and nodal knots^{28,31} (Fig. 1d). Nodal rings, or the ordinary nodal loops, are relatively trivial due to the lack of global topological structures. A nontrivial representative of NL is nodal link, namely, several NLs topologically linked with each other. In comparison, a nodal knot represents a single NL ‘linked’ with itself^{28,31}. With several NLs touching together, nodal chains serve as the transition phase between nodal rings and nodal links/knots³³.

Besides their interesting topological configurations, materials possessing NL links exhibit some very interesting observables, such as, diverse surface state variations, more complicated Landau-level structures, intriguing electromagnetic properties, thermal transports, etc^{28,29}. The first theoretical model of linked NLs has been proposed via inverse Hopf mapping, i.e. the preimage of two different points on the unit 2-sphere is two linked loops in the three-dimensional momentum space^{29-31,38,39}. However, its material realization is very challenging due to its subtle but complicated Hamiltonian form. Therefore, it is urgent and important to find the nodal links/knots in realistic materials. Here, we demonstrate nodal links formed by three bands in a biaxial hyperbolic metamaterial. The system possesses two perpendicular NLs which thread through each other and form linked NLs as shown in Fig. 1e. We further observe the surface bound states in the continuum (BICs) that serve as important features of the linked NL systems.

We start from an effective medium description of the biaxial hyperbolic metamaterial (see Supplementary Materials Section 1). The effective relative permittivity tensor takes the form of $\vec{\epsilon} = \text{diag}[\epsilon_x(\omega), \epsilon_y, \epsilon_z]$, where along x direction the system exhibits a Drude type of dispersion as $\epsilon_x(\omega) = \epsilon_{x\infty} \left(1 - \frac{\omega_p^2}{\omega^2}\right)$ (for simplicity ω_p is normalized to be 1 in the following discussion), while along the other two directions the relative permittivity constants are positive and different, satisfying $\epsilon_y > \epsilon_{x\infty} > \epsilon_z$. The real diagonal form of $\vec{\epsilon}$ indicates that the model possesses mirror symmetries M_x, M_y, M_z , inversion symmetry P and time-reversal symmetry T . The PT symmetry further ensures that the eigen electromagnetic states are all linearly polarized, which will greatly facilitate the following NL characterizations. Along k_x direction, the dispersion of the one-dimensional band structure features a flat band of longitudinal mode (L) with $\omega_L = 1$ and two transverse modes, T_1 and T_2 , with linear

polarization along z and y direction and the dispersion relation $\frac{k_x}{\sqrt{\epsilon_z}}$ and $\frac{k_x}{\sqrt{\epsilon_y}}$, respectively (Fig. 1f). The mirror eigenvalues of the longitudinal mode and the two transverse modes T_1 and T_2 are given by $(+, +)$, $(+, -)$ and $(-, +)$ respectively as shown in Fig. 1f. The first and the second indices represent the eigenvalues of M_y and M_z , respectively.

Due to the orthogonality among the longitudinal mode and the two transverse modes, they form one degeneracy point between the two transverse modes at Γ , and two pairs of degeneracy points between the longitudinal mode and one of the transverse modes at (P_1, P_1') and (P_2, P_2') located at $k_x = \pm\sqrt{\epsilon_z}$ and $\pm\sqrt{\epsilon_y}$, respectively. The degeneracy points Γ , P_2 and P_2' are formed between the first and the second bands and protected by M_y , therefore they are located on the same degeneracy loop on the $k_y = 0$ plane (red in Fig. 1e). On the other hand, the degeneracy points P_1 and P_1' are formed by the second and the third bands and protected by M_z , and they form another degeneracy loop on the $k_z = 0$ plane (blue in Fig. 1e). The interlaced distribution between these five degeneracy points indicates that the two nodal loops they belong to are linked, which is confirmed by theoretically calculated configuration of the nodal lines in the momentum space in Fig. 1e. The NLs are stable and distinct from trivial NLs due to the linking configuration. As the linked nodal lines both involve the 2nd band (thick black line in Fig. 1f) in their construction, we show the corresponding electric field polarization distributions of the 2nd band in Fig. 1g and 1h on the $k_y = 0$ and $k_z = 0$ planes, respectively. One can clearly see that the electric fields abruptly change across the nodal lines because they are protected by the corresponding mirror symmetry but carrying opposite eigenvalues. Around the nodal line, such as the blue/red point in Fig. 1g/h, the electric fields accumulate a Berry phase of π with polarization singularity located on the blue/red point (see details in Supplementary Materials Section 2, Fig. S1).

To illustrate the formation of the nodal lines in more details, we calculate the two-dimensional band structures of the biaxial hyperbolic metamaterial on the $k_y = 0$ and $k_z = 0$ planes based on the Hamiltonian formulation (Eq. S1), which are shown in Fig. 2a and 2b, respectively. On the $k_y = 0$ plane, the first and the second bands cross each other forming an 8-shaped nodal line in the k -space, as indicated by the red solid line in Fig. 2a. The nodal line is highly dispersive though, spanning the whole frequency range from DC to the plasma frequency. The electromagnetic field of the two crossing bands on the $k_y = 0$ plane takes the forms of $[E_x \ 0 \ E_z \ 0 \ H_y \ 0]$ and $[0 \ E_y \ 0 \ H_x \ 0 \ H_z]$, which are the eigenstates of M_y with eigenvalues +1 and -1 respectively, meaning that the nodal line is M_y protected. Due to the dispersive nature of the nodal line, at any frequency between zero and plasma frequency, there exist four nodal points. The Equi-Frequency Contours (EFCs) at two different frequencies 0.4 and 0.8 are shown in Fig. 2c and 2d respectively. The EFCs resemble that of uniaxial hyperbolic media except for that the two quadratic touching points between the TE and TM modes in the uniaxial hyperbolic media are replaced by four linearly touching points. These linear touching points are the nodal points that form the nodal line with continuously varying frequencies. Viewing from the k_y direction, there exists an eye-shaped void in the EFC between each pair of nodal points.

At frequencies above ω_L , the second and the third bands cross each other on the $k_z = 0$ plane, as shown in Fig. 2b. The crossing nodes form a circle in k -space as indicated by the blue solid line in Fig. 2b. The fields of these two crossing bands have the forms $[0 \ 0 \ E_z \ H_x \ H_y \ 0]$ and $[E_x \ E_y \ 0 \ 0 \ 0 \ H_z]$, which are the eigenstates of M_z with eigenvalues are -1 and +1 respectively, i.e. this nodal line is M_z protected. As shown in Fig. 2e and 2f, the corresponding EFC at a given frequency consists of two ellipsoids touching each other at four nodal points, which form

the circular nodal line between the second and the third bands as the frequency continuously varies. Similar EFC has been extensively studied in biaxial crystals, in the context of conical refraction at the nodal points⁴⁰⁻⁴³. When plotting the above two nodal lines together in the k -space as shown in Fig. 1e, it is clearly seen that they are linked with each other. In addition, there are two more nodal lines located on the $k_x = 0$ plane, which tangentially touch the circular nodal line, forming two nodal chains in the k -space (see black lines in Fig. S1a-c). However, because they do not contribute to the formation of the nodal link, they are not the focus of the present work. By further introducing dispersion along y direction, and by tuning the dispersion parameters, various nodal line configurations including nodal links, nodal chains and separated nodal loops can be formed as shown in Fig. S2. Their detailed configurations and the corresponding symmetry analysis are provided in Supplementary Materials Section 3.

To demonstrate the nodal links in experiment, we design a microwave metamaterial that consists of the combination of an array of thin metallic wires and metallic cross structures patterned on a dielectric plate, as shown schematically in Fig. 3a (space group No. 47: Pmmm). The relative permittivity of the dielectric plate is 4.1. The continuous metallic wire provides the Drude-like dispersion-along x direction. The cross structures with arms along $x = \pm y$ orientations provide the anisotropy in the y and z directions. The entire sample contains $75 \times 75 \times 52$ unite cells with periods $p_x = p_y = 4mm$ and $p_z = 3mm$. The bulk modes propagating in the metamaterial is simulated by using a commercially available software - CST Microwave Studio. The simulated dispersion curve along k_x direction is shown in Fig. 3b. The dispersion appears similar to that of the effective medium in Fig. 1f, except for the presence of dispersion in the longitudinal mode due to nonlocal effect⁴⁴. The locations of nodal lines in the k -space are obtained via simulation and shown in Fig. 3c (solid lines). Being the same to

the effective media analysis (Fig. 1e), the realistic metamaterial structure possesses two nodal lines that are linked to each other.

The bulk states of the metamaterial are probed by using the near-field scanning setup (Supplementary Materials Section 7, Fig. S5). The measured complex fields are subsequently Fourier transformed to obtain their distribution in the k -space. The projected EFCs onto the k_x - k_z plane at three different frequencies are shown in Fig. 3d-f. As a reference, the projection of the boundary of the bulk states simulated by CST are also provided in the form of white solid lines. At each frequency, four nodal points together with the eye-shaped voids are clearly visible in the EFC. The continuous variation of these nodal points over frequency forms the 8-shaped nodal line on the $k_y = 0$ plane in Fig. 3c. The projected EFCs onto the k_x - k_y plane at three higher frequencies are shown in Fig. 3g-i, which features two elliptically shaped contours intercepting each other at four points. The continuous variation of the four interception points at different frequencies forms the circular nodal line on the $k_z = 0$ plane. Further results from the measurements of bulk states directly confirm the presence of linked nodal lines as shown in Fig. S6-7 (Supplementary Materials Section 8). Their positions are labelled in Fig. 3c. Hence the existence of the nodal links is verified experimentally.

For systems possessing nodal line degeneracies, there may exist drumhead surface states^{2,5,8,10,45,46}. To explore the surface states of the metamaterial, a slightly different measurement configuration is employed (Supplementary Materials Section 7, Fig. S5d and S5e). We measure the surface states for both the interfaces in the x - z plane and that in the x - y plane. For the interface in the x - z plane, the dispersion of surface state along k_x direction together with the simulation result is shown in Fig. 4a (see the analytical results based on the effective media analysis in Supplementary Materials Section 4, Fig. S3a). It is shown that the

dispersion of the surface state along the k_x direction is asymptotical to the free space dispersion of air at very low frequencies. It becomes more curved at higher frequencies and eventually terminates at point P_2 . The dispersion curve is divided into two sections, that with k_x less than the T_1 mode (coloured in green), and that with k_x greater than the T_1 mode (coloured in magenta). These two sections in green and magenta colour represent the surface BIC⁴⁷⁻⁵¹ and normal surface state, respectively. Both the simulated and measured dispersion curves show similar features as that calculated based on effective medium approximation (Fig. S3a). The probed EFCs of the surface states with different frequencies are shown in Fig. 4c-e. At each frequency, there are two bright spots that correspond to the surface BICs, whose locations coincide well with the simulation results, as indicated by the green circular points. With the increase of frequency, the surface BICs move further away from the light cone, indicating a stronger confinement on the air side. Detailed analysis of the surface states in the Supplementary Materials Section 5 shows that the surface BICs are essentially the symmetry-enforced extension of the drumhead surface states from nodal links.

For the interface in the x - y plane, the measured and simulated dispersion curves of the surface BIC along k_x direction are shown in Fig. 4b. The surface BIC from both the simulation and the measurement connects between Γ point and P_1 point, which agrees well with that of the effective medium analysis (Supplementary Materials Section 4-5, Fig. S3e). Figure 4(f-h) present the surface states at three different frequencies. The surface BICs are indicated by the isolated bright spots on the k_x axis. Besides the surface BIC, the normal surface state in the form of Fermi arcs are also observed that connect between the projections of the nodal points and the EFC of the bulk states. Again, the above features agree very well with the effective medium description provided in Supplementary Materials Section 5 (Fig. S3). Detailed

analysis about propagating constants of surface states is given in Supplementary Materials Section 6 (Fig. S4).

To summarize, we designed and realised a nodal link metamaterial based on effective media theory. The presence of the nodal links involves the crossings between three adjacent bands, which includes three modes: one longitudinal mode and two transverse modes in two orthogonal planes in the momentum space. Both the linked nodal lines and the presence of surface BICs are experimentally confirmed. Further introduction of dispersion to the permittivity tensor elements along different directions may allow observation of more exotic nodal line configurations. Our work also serves as a link between the recently discovered nodal-line topological systems to well-known phenomenon of conical refraction in biaxial birefringent crystals that has been studied for centuries.

References

- 1 Wan, X., Turner, A. M., Vishwanath, A. & Savrasov, S. Y. Topological semimetal and Fermi-arc surface states in the electronic structure of pyrochlore iridates. *Physical Review B* **83**, 205101, doi:10.1103/PhysRevB.83.205101 (2011).
- 2 Burkov, A. A., Hook, M. D. & Balents, L. Topological nodal semimetals. *Physical Review B* **84**, doi:10.1103/PhysRevB.84.235126 (2011).
- 3 Lu, L., Fu, L., Joannopoulos, J. D. & Soljačić, M. Weyl points and line nodes in gyroid photonic crystals. *Nature Photonics* **7**, 294, doi:10.1038/nphoton.2013.42 <https://www.nature.com/articles/nphoton.2013.42 - supplementary-information> (2013).
- 4 Xiao, M., Chen, W.-J., He, W.-Y. & Chan, C. T. Synthetic gauge flux and Weyl points in acoustic systems. *Nature Physics* **11**, 920, doi:10.1038/nphys3458 <https://www.nature.com/articles/nphys3458 - supplementary-information> (2015).
- 5 Weng, H. *et al.* Topological node-line semimetal in three-dimensional graphene networks. *Physical Review B* **92**, doi:10.1103/PhysRevB.92.045108 (2015).
- 6 Xiao, M., Lin, Q. & Fan, S. Hyperbolic Weyl Point in Reciprocal Chiral Metamaterials. *Phys Rev Lett* **117**, 057401, doi:10.1103/PhysRevLett.117.057401 (2016).
- 7 Bzdusek, T., Wu, Q., Ruegg, A., Sigrist, M. & Soluyanov, A. A. Nodal-chain metals. *Nature* **538**, 75-78, doi:10.1038/nature19099 (2016).
- 8 Fang, C., Weng, H., Dai, X. & Fang, Z. Topological nodal line semimetals. *Chinese Physics B* **25**, doi:10.1088/1674-1056/25/11/117106 (2016).
- 9 Guo, Q. *et al.* Three Dimensional Photonic Dirac Points in Metamaterials. *Phys Rev Lett* **119**, 213901, doi:10.1103/PhysRevLett.119.213901 (2017).
- 10 Kawakami, T. & Hu, X. Symmetry-guaranteed nodal-line semimetals in an fcc lattice. *Physical Review B* **96**, doi:10.1103/PhysRevB.96.235307 (2017).
- 11 Noh, J. *et al.* Experimental observation of optical Weyl points and Fermi arc-like surface states. *Nature Physics* **13**, 611, doi:10.1038/nphys4072 <https://www.nature.com/articles/nphys4072 - supplementary-information> (2017).
- 12 Armitage, N. P., Mele, E. J. & Vishwanath, A. Weyl and Dirac semimetals in three-dimensional solids. *Reviews of Modern Physics* **90**, 015001, doi:10.1103/RevModPhys.90.015001 (2018).

- 13 Yan, Q. *et al.* Experimental discovery of nodal chains. *Nature Physics* **14**, 461-464, doi:10.1038/s41567-017-0041-4 (2018).
- 14 Tan, X. *et al.* Demonstration of Hopf-link semimetal bands with superconducting circuits. *Applied Physics Letters* **112**, 172601, doi:10.1063/1.5029439 (2018).
- 15 Gao, W. *et al.* Experimental observation of photonic nodal line degeneracies in metacrystals. *Nature Communications* **9**, 950, doi:10.1038/s41467-018-03407-5 (2018).
- 16 Wang, D. *et al.* Photonic Weyl points due to broken time-reversal symmetry in magnetized semiconductor. *Nature Physics*, doi:10.1038/s41567-019-0612-7 (2019).
- 17 Chang, G. *et al.* Topological Hopf and Chain Link Semimetal States and Their Application to $\text{Co}_{\{2\}}\text{MnGa}$. *Phys Rev Lett* **119**, 156401, doi:10.1103/PhysRevLett.119.156401 (2017).
- 18 Takahashi, R., Hirayama, M. & Murakami, S. Spinless hourglass nodal-line semimetals. *Physical Review B* **96**, doi:10.1103/PhysRevB.96.155206 (2017).
- 19 Xia, L. *et al.* Observation of Hourglass Nodal Lines in Photonics. *Physical Review Letters* **122**, 103903, doi:10.1103/PhysRevLett.122.103903 (2019).
- 20 Lu, L., Fu, L., Joannopoulos, J. D. & Soljačić, M. Weyl points and line nodes in gyroid photonic crystals. *Nature Photonics* **7**, 294-299, doi:10.1038/nphoton.2013.42 (2013).
- 21 Yu, R., Weng, H., Fang, Z., Dai, X. & Hu, X. Topological Node-Line Semimetal and Dirac Semimetal State in Antiperovskite Cu_3PdN . *Phys Rev Lett* **115**, 036807, doi:10.1103/PhysRevLett.115.036807 (2015).
- 22 Okugawa, R. & Murakami, S. Universal phase transition and band structures for spinless nodal-line and Weyl semimetals. *Physical Review B* **96**, doi:10.1103/PhysRevB.96.115201 (2017).
- 23 Yu, R., Wu, Q., Fang, Z. & Weng, H. From Nodal Chain Semimetal to Weyl Semimetal in HfC . *Phys Rev Lett* **119**, 036401, doi:10.1103/PhysRevLett.119.036401 (2017).
- 24 Zhang, T. T. *et al.* From Type-II Triply Degenerate Nodal Points and Three-Band Nodal Rings to Type-II Dirac Points in Centrosymmetric Zirconium Oxide. *J Phys Chem Lett* **8**, 5792-5797, doi:10.1021/acs.jpcclett.7b02642 (2017).
- 25 Gao, W. *et al.* Experimental observation of photonic nodal line degeneracies in metacrystals. *Nat Commun* **9**, 950, doi:10.1038/s41467-018-03407-5 (2018).

- 26 Deng, W. *et al.* Nodal rings and drumhead surface states in phononic crystals. *Nat Commun* **10**, 1769, doi:10.1038/s41467-019-09820-8 (2019).
- 27 Liu, Q. B., Fu, H. H., Xu, G., Yu, R. & Wu, R. Categories of Phononic Topological Weyl Open Nodal Lines and a Potential Material Candidate: Rb₂Sn₂O₃. *J Phys Chem Lett* **10**, 4045-4050, doi:10.1021/acs.jpcclett.9b01159 (2019).
- 28 Bi, R., Yan, Z., Lu, L. & Wang, Z. Nodal-knot semimetals. *Physical Review B* **96**, 201305, doi:10.1103/PhysRevB.96.201305 (2017).
- 29 Yan, Z. *et al.* Nodal-link semimetals. *Physical Review B* **96**, doi:10.1103/PhysRevB.96.041103 (2017).
- 30 Chen, W., Lu, H.-Z. & Hou, J.-M. Topological semimetals with a double-helix nodal link. *Physical Review B* **96**, doi:10.1103/PhysRevB.96.041102 (2017).
- 31 Ezawa, M. Topological semimetals carrying arbitrary Hopf numbers: Fermi surface topologies of a Hopf link, Solomon's knot, trefoil knot, and other linked nodal varieties. *Physical Review B* **96**, doi:10.1103/PhysRevB.96.041202 (2017).
- 32 Ahn, J., Kim, D., Kim, Y. & Yang, B.-J. Band Topology and Linking Structure of Nodal Line Semimetals with $\{Z\}_2$ Monopole Charges. *Physical Review Letters* **121**, 106403, doi:10.1103/PhysRevLett.121.106403 (2018).
- 33 Yang, Z., Chiu, C.-K., Fang, C. & Hu, J. Evolution of nodal lines and knot transitions in topological semimetals. *arXiv:1905.00210 [cond-mat.mes-hall]* (2019).
- 34 Xie, Y., Cai, J., Kim, J., Chang, P.-Y. & Chen, Y. Hopf-chain networks evolved from triple points. *Physical Review B* **99**, 165147, doi:10.1103/PhysRevB.99.165147 (2019).
- 35 Liu, Z. *et al.* Experimental Observation of Dirac Nodal Links in Centrosymmetric Semimetal TiB_2 . *Physical Review X* **8**, 031044, doi:10.1103/PhysRevX.8.031044 (2018).
- 36 Lou, R. *et al.* Experimental observation of bulk nodal lines and electronic surface states in ZrB₂. *npj Quantum Materials* **3**, 43, doi:10.1038/s41535-018-0121-4 (2018).
- 37 Gong, C., Xie, Y., Chen, Y., Kim, H.-S. & Vanderbilt, D. Symmorphic Intersecting Nodal Rings in Semiconducting Layers. *Physical Review Letters* **120**, 106403, doi:10.1103/PhysRevLett.120.106403 (2018).
- 38 Lyons, D. W. An Elementary Introduction to the Hopf Fibration. *Mathematics Magazine* **76**, doi:10.2307/3219300 (2003).

- 39 Moore, J. E., Ran, Y. & Wen, X. G. Topological surface States in three-dimensional magnetic insulators. *Phys Rev Lett* **101**, 186805, doi:10.1103/PhysRevLett.101.186805 (2008).
- 40 C.V.RAMAN. Conical Refraction in Biaxial Crystals. *Nature* **107**, 747 (1921).
- 41 Turpin, A., Loiko, Y. V., Kalkandjiev, T. K. & Mompert, J. Conical refraction: fundamentals and applications. *Laser & Photonics Reviews* **10**, 750-771, doi:10.1002/lpor.201600112 (2016).
- 42 Lunney, J. G. & Weaire, D. The ins and outs of conical refraction. *Europhysics News* **37**, 26-29, doi:10.1051/eprn:2006305 (2006).
- 43 Saad, F. & Belafhal, A. A detailed study of internal conical refraction phenomenon of Flattened Gaussian beams propagating in a biaxial crystal. *Optik* **138**, 145-152, doi:10.1016/j.ijleo.2017.03.038 (2017).
- 44 Demetriadou, A. & Pendry, J. B. Taming spatial dispersion in wire metamaterial. *Journal of Physics: Condensed Matter* **20**, 295222, doi:10.1088/0953-8984/20/29/295222 (2008).
- 45 Gao, W.-L., Fang, F.-Z., Liu, Y.-M. & Zhang, S. Chiral surface waves supported by biaxial hyperbolic metamaterials. *Light: Science & Applications* **4**, e328-e328, doi:10.1038/lsa.2015.101 (2015).
- 46 Bian, G. *et al.* Drumhead surface states and topological nodal-line fermions in TiTaSe_2 . *Physical Review B* **93**, doi:10.1103/PhysRevB.93.121113 (2016).
- 47 Plotnik, Y. *et al.* Experimental observation of optical bound states in the continuum. *Phys Rev Lett* **107**, 183901, doi:10.1103/PhysRevLett.107.183901 (2011).
- 48 Hsu, C. W. *et al.* Bloch surface eigenstates within the radiation continuum. *Light: Science & Applications* **2**, e84-e84, doi:10.1038/lsa.2013.40 (2013).
- 49 Zhen, B., Hsu, C. W., Lu, L., Stone, A. D. & Soljacic, M. Topological nature of optical bound states in the continuum. *Phys Rev Lett* **113**, 257401, doi:10.1103/PhysRevLett.113.257401 (2014).
- 50 Hsu, C. W., Zhen, B., Stone, A. D., Joannopoulos, J. D. & Soljačić, M. Bound states in the continuum. *Nature Reviews Materials* **1**, doi:10.1038/natrevmats.2016.48 (2016).
- 51 Doleman, H. M., Monticone, F., den Hollander, W., Alù, A. & Koenderink, A. F. Experimental observation of a polarization vortex at an optical bound state in the continuum. *Nature Photonics* **12**, 397-401, doi:10.1038/s41566-018-0177-5 (2018).

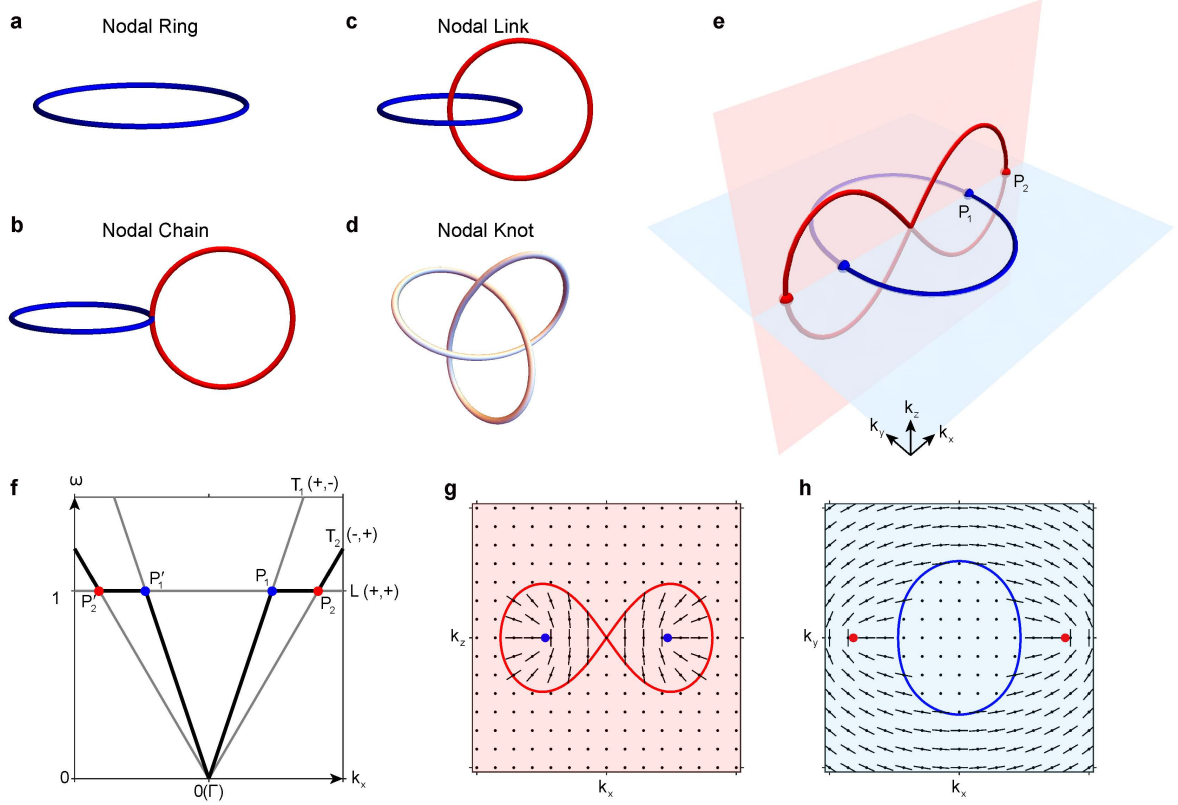


Figure 1 | Nodal links in biaxial hyperbolic metamaterials. **a**, Nodal rings. **b**, Nodal chain. **c**, Nodal link. **d**, Nodal knot. **e**, Nodal links in biaxial hyperbolic metamaterials. The effective parameters of the system are $\epsilon_y = 6$, $\epsilon_z = 2$ and $\epsilon_x(\omega) = \epsilon_{x\infty} \left(1 - \frac{\omega_p^2}{\omega^2}\right)$ with $\epsilon_{x\infty} = \frac{11}{2}$. **f**, Band structure along k_x direction shows four crossing points (P'_1, P'_2, P_1, P_2) between one longitudinal mode L and two transverse modes T_1 and T_2 . The second band is highlighted by thick black line. ω is normalized by ω_p . **g**, Calculated linear-polarized electric field distribution on the $k_y = 0$ plane. **h**, Similar to **g** but on the $k_z = 0$ plane.

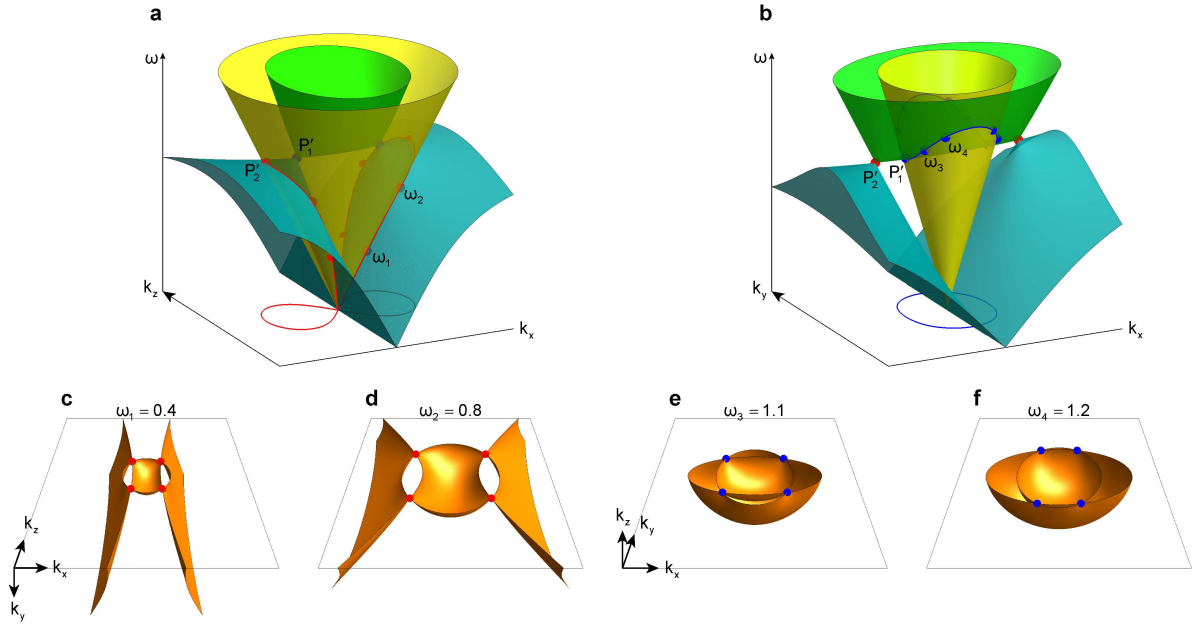


Figure 2 | Nodal links via the crossings between three adjacent bands. **a** and **b**, Two-dimensional band structures of biaxial hyperbolic metamaterial on the $k_y = 0$ and $k_z = 0$ planes, respectively. The nodal lines formed by band crossings and their projections onto the k -plane are denoted by the red/blue solid lines. **c** and **d**, Equi-Frequency Contours (EFCs) at $\omega_1 = 0.4$ and $\omega_2 = 0.8$, respectively. **e** and **f**, EFCs at $\omega_3 = 1.1$ and $\omega_4 = 1.2$, respectively. The half of each EFC has been cut off for clearly see the structure inside.

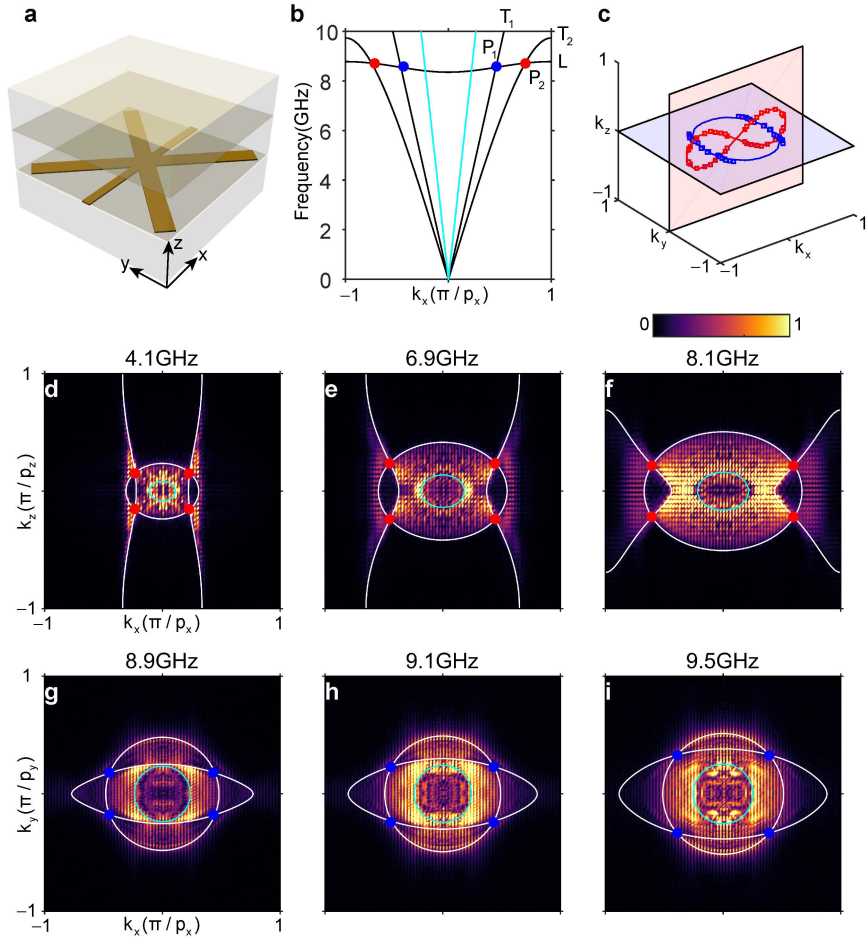


Figure 3 | Experimental demonstration of nodal links in biaxial hyperbolic metamaterial.

a, Schematic diagram of the unit cell, belonging to the space group No. 47: Pmmm. The metallic structure is made of copper with a thickness of 0.035mm. The width of the connective metallic wire is 0.2mm. The length and width of each arm of the metallic cross structure are 5mm and 0.4mm, respectively. **b**, The simulated bulk dispersion curve along k_x direction. **c**, The experimentally probed (square dots) and the numerically simulated nodal lines (solid lines) in the k -space. **d-f** and **g-i**, The projected Equi-Frequency Contours (EFCs) with respect of

different frequencies on the k_x - k_z and k_x - k_y planes, respectively. White/cyan solid line corresponds to the projected bulk state boundary of the biaxial hyperbolic metamaterial/air.

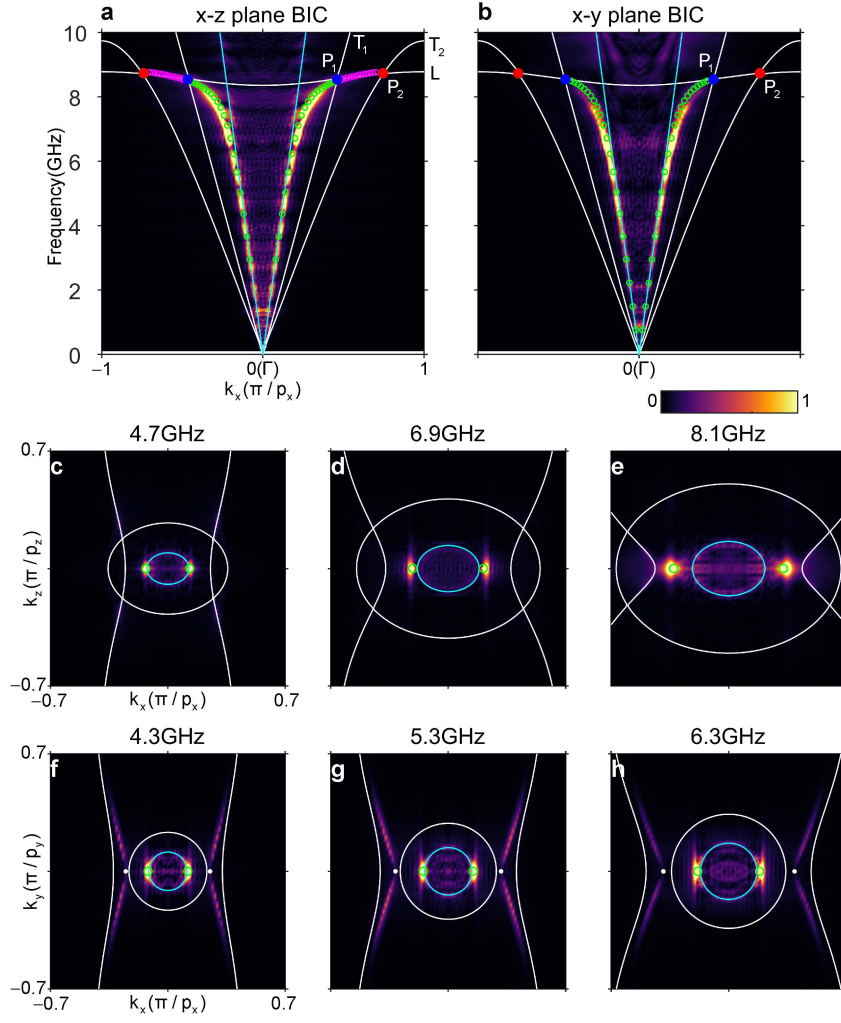


Figure 4 | Experimental observation of surface bound state in the continuum (BIC). **a** and **b**, The measured dispersion of surface state along k_x direction in the interfaces of x - z and x - y planes, respectively. Green and magenta circles indicate the simulated surface BICs and normal surface states, respectively. **c-e**, and **f-h**, Equi-Frequency Contours (EFCs) of surface states with respect of three different frequencies on the interfaces x - z and x - y planes, respectively. The white dots in **f-h** denote the projection of nodal points. Green circles indicate

the surface BICs. White/cyan solid line corresponds to the projected bulk state boundary of the biaxial hyperbolic metamaterial/air.